

2021-08-01

Computational Investigation Of Nanoparticle Immersion And Selfassembly

Tara Allison Tyler Nitka
University of Texas at El Paso

Follow this and additional works at: https://scholarworks.utep.edu/open_etd



Part of the [Physical Chemistry Commons](#)

Recommended Citation

Nitka, Tara Allison Tyler, "Computational Investigation Of Nanoparticle Immersion And Selfassembly" (2021). *Open Access Theses & Dissertations*. 3307.
https://scholarworks.utep.edu/open_etd/3307

This is brought to you for free and open access by ScholarWorks@UTEP. It has been accepted for inclusion in Open Access Theses & Dissertations by an authorized administrator of ScholarWorks@UTEP. For more information, please contact lweber@utep.edu.

COMPUTATIONAL INVESTIGATION OF NANOPARTICLE IMMERSION AND SELF-
ASSEMBLY

TARA ALLISON TYLER NITKA

Doctoral Program in Chemistry

APPROVED:

Lela Vuković, Ph.D., Chair

Dino Villagrán, Ph.D.

Sreeprasad Sreenivasan, Ph.D.

Tunna Baruah, Ph.D.

Stephen L. Crites, Jr., Ph.D.
Dean of the Graduate School

Copyright ©

by

Tara Nitka

2021

Dedication

This dissertation is for the birds. They deserve much more recognition than they get for being the best part of the biosphere.

COMPUTATIONAL INVESTIGATION OF NANOPARTICLE IMMERSION AND SELF-
ASSEMBLY

by

TARA ALLISON TYLER NITKA, B.Sc.

DISSERTATION

Presented to the Faculty of the Graduate School of

The University of Texas at El Paso

in Partial Fulfillment

of the Requirements

for the Degree of

DOCTOR OF PHILOSOPHY

Department of Chemistry and Biochemistry

THE UNIVERSITY OF TEXAS AT EL PASO

August 2021

Acknowledgements

I thank my adviser, Prof. Lela Vuković, for her guidance and support during my doctoral research and the preparation of this dissertation. I also thank Prof. Petr Král at the University of Illinois at Chicago for his advice and discussions. I thank the Texas Advanced Computing Center (TACC) and the Blue Waters project at the National Center for Supercomputing Applications for computational resources. Finally, I thank the Department of Chemistry and Biochemistry at the University of Texas at El Paso for supporting this research under startup funding and the National Institutes of Health for supporting our research on virucidal NPs under grant number 1 R03 AI142553-01.

Abstract

Both neutral and charged nanoparticles with a variety of compositions, shapes, and sizes have been previously prepared. These nanoparticles have been demonstrated to self-assemble into a variety of superlattices and binary superlattices both in bulk solution and at surfaces of solutions, and the structures formed by self-assembly have been shown to depend on nanoparticle chemistry and charge as well as on whether assembly takes place at a surface or in bulk. Furthermore, the prepared isolated and self-assembled nanoparticles have a number of biomedical, nanotechnology, and industrial applications. In this dissertation, I present my research on three general topics. First, I will present my research on neutral nanocube immersion and self-assembly at the liquid-air interface. Here, the self-assembly of neutral nanocubes at a water surface is shown to depend on ligand hydrophobicity. Second, I will present my computational research on a project performed in collaboration with experimental group, related to self-assembly of supercharged nanoparticles. A phase diagram showing the dependence of superlattice structure on nanoparticle size ratio for charged spherical nanoparticles in bulk solution is developed. I will finally present the computational component of research I performed in collaboration with experimental colleagues on the assembly of carbon nanotube-DNA nanosensors which use a DNA-bound peptide to recognize proteins.

Table of Contents

Acknowledgements.....	v
Abstract.....	vi
Table of Contents.....	vii
List of Figures.....	ix
Chapter 1: Introduction.....	1
Self-assembled nanoparticle superlattices.....	1
Functionalization of carbon nanotubes as biosensors.....	1
Chapter 2: Methods.....	3
Classical molecular dynamics.....	3
Force fields.....	3
Integration methods.....	5
Periodic boundary conditions.....	6
Ensembles.....	6
Simulation parameters.....	7
Umbrella sampling.....	8
Chapter 3: Nanocube immersion and clustering at the water-air interface.....	9
Introduction.....	9
Methods.....	10
Analytical model.....	10
MD simulations.....	11
Data analysis.....	11
Results.....	12
Analytical model of nanocube immersion.....	12
MD simulations.....	13
Conclusions.....	16
Chapter 4: Self-assembly of super-charged nanospheres in ionic solution.....	17
Introduction.....	17
Methods.....	18

Geometric criterion for superlattice structure	18
Numerical model of superlattice structure using free energy profiles	19
Results	20
Geometric criterion for lattice formation	20
Numerical model of lattice formation based on Gibbs free energy	21
Conclusions	23
Chapter 5: Computational modeling of carbon nanotube-bound DNA-peptide conjugate nanosensors	24
Introduction	24
Methods	24
Results	27
Conclusions	28
References	29

Vita 38

List of Figures

Figure 3.1: Analytical model of NP immersion. For the flat orientation minima are possible only at full immersion and zero immersion, while for the tilted orientation a local or global minimum near half immersion is observed.	11
Figure 3.2: Configurations of A) hydrophobic NC, B) moderately hydrophilic NC, and C) hydrophilic NC on water (transparent blue surface) surface after 100 ns MD simulation. D-F) Configurations of NCs with similar hydrophobicity to A-C but with explicit ligands (C atoms shown in green, O atoms in red, and H atoms not shown for clarity). G) Immersed area of naked NCs as a function of ϵ . H) Angle between naked NC body diagonal and vector normal to liquid surface as function of ϵ . NC immersion depends on the hydrophobicity of the NC.	15
Figure 3.3: A) Configurations of two or three NC clusters ($\epsilon = -0.3$ kcal/mol) in different initial arrangements (insets). In the initial states, the NCs have 45 or 50 Å center-to-center distances. B) Configurations of four NC clusters ($\epsilon = -0.3$ kcal/mol) in different initial arrangements (insets). In the initial state, the NCs have 45 Å center-to-center distances. All images are obtained after 100 ns of equilibration.	16
Figure 4.1: Scheme of A) CsCl, B) hexagonal, and C) Th ₃ P ₄ lattices showing their respective lattice constants.....	19
Figure 4.2: A) A pair of Au@TMA (left) and Au@MUA (right) NPs in 4.28 M (NH ₄) ₂ CO ₃ solution, after 22 ns of equilibration. TMA is shown in blue, 1-hexanethiol in cyan, MUA in green, NH ₄ ⁺ ions in dark blue, and CO ₃ ²⁻ ions in red. NP cores are 5 nm in diameter and NPs are shown at a center-to-center distance of 7.3 nm. B) The free energy profiles of NP binding as calculated by US for each pair of NPs.	20

Figure 4.3: Phase diagram of self-assembled superlattice structures, obtained in experiment by Prof. Rafal Klajn's group (points) superposed with the line boundaries obtained by the geometric criteria analytical model. The variables are the sizes of the positively and negatively charged particles. 21

Figure 4.4: Contour maps showing lattice free energy surfaces of (a) CsCl, (b-c) hexagonal, and (d-e) Th₃P₄ lattices, overlaid with experimental data from the Klajn group (points). 23

Figure 4.5: Phase diagram of SL formation by Au@MUA and Au@TMA NPs in aqueous 4.28 M (NH₄)₂CO₃ solution, overlaid with experimental data. 23

Figure 5.1: a) linear hybrid structure; b) bridged hybrid structure; c) RGD solvent exposed fraction; d) binding of RGD motif to integrin $\alpha_{\text{IIb}}\beta_3$ 26

Figure 5.2: Plots of the normalized position of RGD in cylindrical coordinates, for a) r; b) θ ; c) z. The r coordinate is correlated with RGD binding availability. 27

Chapter 1: Introduction

In this dissertation, I describe my research in two broad areas of computational modeling of self-assembled nanomaterials. These materials are built from ligated metallic nanoparticles or from carbon nanotubes wrapped with biological macromolecules.

SELF-ASSEMBLED NANOPARTICLE SUPERLATTICES

Experimentalists have synthesized nanoparticles (NPs) with a variety of compositions^{1,2}, sizes³⁻⁵, and shapes⁶⁻¹¹, and have prepared superlattices resulting from self-assembly of a wide variety of these NPs in bulk solution^{12,13} and on the surface of solutions¹⁴⁻¹⁸. The resulting superlattices have novel electrical, thermal, optical, and magnetic properties resulting from their nanoscale structure¹⁸⁻²¹. It has been demonstrated that the structures formed are dependent on NP geometry and chemistry¹, whether self-assembly takes place in bulk solution or on a surface¹², and whether NPs are neutral or charged^{20,22}. Investigation of self-assembly processes is needed to understand how superlattice structure is determined and will facilitate the development of novel superlattices with desirable properties. Here, I present my research efforts employing molecular dynamics (MD) simulations and analytical modeling to understand the self-assembly of cubic NPs at liquid surfaces and the self-assembly of charged spherical NPs in bulk solution.

FUNCTIONALIZATION OF CARBON NANOTUBES AS BIOSENSORS

Carbon nanotubes are another subset of nanomaterials with interesting applications based on their unique photophysical properties and 1-dimensional geometry²³⁻²⁶. Since their discovery, they have been investigated as components of bioimaging systems and as a basis for nanoscale therapies^{27,28}. Single walled carbon nanotubes (SWCNTs) are rolled carbon monolayers with structure described by their chirality index (n,m) , which determines their photophysical properties,

and semiconducting SWCNTs have a band gap that results in near infrared (nIR) fluorescence (850-1700 nm)²⁹, making them particularly useful for bioimaging applications³⁰. Use of these SWCNTs in functional materials is an area of current interest, as most of the chemical modifications used when SWCNTs are included in functional materials destroy their nIR fluorescence due to distortion of the conjugated π system³¹, making their use as biosensors challenging. Noncovalent modifications such as wrapping of SWCNTs with ssDNA have been shown to produce fluorescent biosensors for reactive oxygen species, small molecules, neurotransmitters, nucleic acids, sugars, and proteins³²⁻³⁴. Here, I describe my use of MD simulations to understand the availability of a peptide bound to 1 or 2 ssDNA molecules for binding to $\alpha_{\text{IIB}}\beta_3$ integrin protein when (6,5)-SWCNTs are functionalized with the peptide-ssDNA hybrid.

Chapter 2: Methods

CLASSICAL MOLECULAR DYNAMICS

The primary technique I have used in this dissertation is the classical molecular dynamics (MD) simulation technique, which I used to perform all the simulations, as well as the umbrella sampling calculations. Classical MD models the time-evolution of a chemical system by integrating Newtonian equations of motion for all particles in the system. For a system consisting of N particles, Newton's equations of motion are:

$$m_i \frac{\partial^2 \vec{r}_i}{\partial t^2} = \vec{f}_i \quad \vec{f}_i = -\frac{\partial}{\partial \vec{r}_i} U(\vec{r}_1, \vec{r}_2, \dots, \vec{r}_N) \quad (2.1)$$

Solving eq. 2.1 requires calculating the forces \vec{f}_i exerted on particle i by all other particles in the system. This requires the mass of particle i (m_i) and the potential energy U , which is a function of $3N$ atomic coordinates $(\vec{r}_1, \vec{r}_2, \dots, \vec{r}_N)$. MD calculations require finding the potential form $U(\vec{r}_1, \vec{r}_2, \dots, \vec{r}_N)$ and efficient numerical integration of eq. 2.1. Potential energy forms in atomistic calculations are approximated using force fields comprising atomic interaction parameters based on quantum mechanical calculations, typically of atoms in a similar chemical environment rather than the atoms in the actual system of interest. The numerical integration of the equations of motion is accomplished using MD software such as NAMD³⁵, which is the software used for all simulations presented in this dissertation.

FORCE FIELDS

The CHARMM36 all-atom (AA) force field³⁶ is used for all simulations presented. Parameterization of atomistic force fields is performed by quantum mechanical calculations³⁶ and parameters are verified by comparison of simulated thermodynamic properties to their experimental values^{37,38}.

Force field parameters comprise bonded parameters which determine intramolecular interaction energies and non-bonded parameters which determine intermolecular interaction energies. The total potential energy of a system is the sum of the bonded and non-bonded interaction energies,

$$V_N = \sum V_{N,bonded} + \sum V_{N,non-bonded} \quad (2.2)$$

For the CHARMM³⁶ force field, the bonded potentials $V_{N,bonded}$ include intramolecular stretching, bending, and torsion interactions. In both cases these are represented by bond, angle, dihedral, and improper dihedral potentials defined as:

$$V_{bond} = \sum_{bond\ i} k_i^{bond} (r_i - r_{0i})^2 \quad (2.3)$$

$$V_{angle} = \sum_{angle\ i} k_i^{angle} (\theta_i - \theta_{0i})^2 \quad (2.4)$$

$$V_{dihedral} = \sum_{dihedral\ i} k_i^{dihedral} [1 + \cos(n_i \phi_i - \gamma_i)], n_i \neq 0 \quad (2.5)$$

$$V_{improper} = \sum_{improper\ i} k_i^{improper} (\phi_i - \gamma_i), n_i \neq 0 \quad (2.6)$$

V_{bond} , V_{angle} and $V_{improper}$ are defined as harmonic potentials and computed using the interaction strength k_i^{bond} , k_i^{angle} or $k_i^{improper}$ and the difference between the instantaneous coordinate r_i , angle θ_i , or improper dihedral ϕ_i and the equilibrium value r_{0i} , θ_{0i} , or γ . The equilibrium values of r , θ , and γ are thus energetic minima associated with stretching, bending, and torsion. $V_{dihedral}$ is defined using a force constant $k_i^{dihedral}$ and a cosine function dependent on dihedral angle ϕ_i , periodicity n_i , and the equilibrium dihedral γ_i . Non-bonded contributions to potential energy consist of electrostatic (Coulomb) and van der Waals (vdW) interactions, both of

which are pair-wise interactions. The long-range Coulomb potential between atoms i and j , which respectively carry charges q_i and q_j , is defined as:

$$V_{Coul}(r_{ij}) = \sum_i \sum_{j>i} \frac{q_i q_j}{4\pi\epsilon_0 r_{ij}} \quad (2.7)$$

In eq. 2.7, ϵ_0 and r_{ij} represent respectively the permittivity of free space and the center-to-center distance of particles i and j . The van der Waals interactions between particles i and j is represented by the short-range Lennard-Jones potential

$$V_{LJ} = \sum_i \sum_{j>i} \epsilon_{ij} \left[\left(\frac{R_{min,ij}}{r_{ij}} \right)^{12} - 2 \left(\frac{R_{min,ij}}{r_{ij}} \right)^6 \right] \quad (2.8)$$

and the values of $R_{min,ij}$ and ϵ_{ij} are determined by the force field using the Lorentz-Berthelot combination rules:

$$R_{min,ij} = \frac{R_{min,i} + R_{min,j}}{2}, \epsilon_{ij} = \sqrt{\epsilon_i \epsilon_j} \quad (2.9)$$

where $R_{min,i}$ and $R_{min,j}$ are the radii of particles i and j , while ϵ_i and ϵ_j are the potential well depths of particles i and j . For all atomistic simulations in this dissertation, interaction parameters from the CHARMM force field are used.

INTEGRATION METHODS

During MD simulations, the positions and velocities of particles are calculated by integration of Newton's equations of motion. One of the algorithms commonly used for this purpose is the Verlet algorithm³⁹ implemented by NAMD³⁵, which recalculates positions and velocities at the same. NAMD implements the Verlet algorithm in the following way³⁵:

$$\begin{aligned} \text{"half-kick"} \quad v_{n+\frac{1}{2}} &= v_n + m^{-1} f_n \cdot \frac{\Delta t}{2} \\ \text{"drift"} \quad R_{n+1} &= R_n + v_{n+\frac{1}{2}} \cdot \Delta t \end{aligned}$$

$$\begin{aligned} \text{“compute force” } f_{n+1} &= f(R_{n+1}) \\ \text{“half-kick” } v_{n+1} &= v_{n+\frac{1}{2}} + m^{-1} f_{n+1} \cdot \frac{\Delta t}{2} \end{aligned}$$

where R_n , v_n , and f_n are the position, velocity, and force associated with a given atom at time step n .

PERIODIC BOUNDARY CONDITIONS

Due to the computational cost of integrating equations of motion for large numbers of particles, current MD packages are limited to simulations involving numbers of particles on the order of 10^7 or fewer. While it is possible to simulate systems involving larger numbers of atoms by using coarse grained force fields, simulations bounded by vacuum will produce non-physical results because they do not accurately represent real systems. To resolve this issue, periodic boundary conditions (PBC) are defined such that the simulation unit cell is repeated periodically along the x, y, and z axes in both the negative and positive directions. This allows the system to interact with its periodic images at the boundaries of the cell rather than showing non-physical behavior as a result of vacuum interfaces.

ENSEMBLES

MD simulations can be conducted in many thermodynamic ensembles, the commonly used ensembles being the microcanonical (NVE) ensemble, the canonical (NVT) ensemble, and the isobaric-isothermal (NPT) ensemble. In the NVE ensemble, number of particles (N), volume (V) and total energy (E) are all held constant, while for the NVT ensemble N, V and temperature (T) are held constant. The NPT ensemble has constant N, pressure (P), and T. Production simulations in this dissertation are conducted in the NVT ensemble, but in some cases the NPT ensemble is used in the preparation of an equilibrated simulation system. There are several techniques used to produce constant temperature simulations, including the Langevin method used by NAMD³⁵. The

Langevin method damps T fluctuations by adding damping and fluctuating terms to the Newtonian equations of motion:

$$m_i \frac{\partial^2 \vec{r}_i}{\partial t^2} = m\dot{v} = F(r) - \gamma_{Lang}mv + \sqrt{2\gamma_{Lang}k_B T_m}G(t) \quad (2.11)$$

where r , t , m , v , and F are respectively defined as position, time, mass, velocity, and force. T , γ_{Lang} , and k_B respectively denote temperature, the Langevin damping factor (defined by the user based on the properties of the system), and the Boltzmann constant. Finally, $G(t)$ represents a univariate Gaussian process. In Eq. 2.11, the second and third terms are respectively the damping and fluctuating terms and have magnitude controlled by γ_{Lang} . Langevin dynamics simulates coupling of the system to a reservoir at a defined temperature T , with the strength of the coupling dependent on γ_{Lang} . For $\gamma_{Lang} = 0$, Langevin dynamics are identical to Newtonian dynamics.

SIMULATION PARAMETERS

In MD simulations, all particles of a system interact through non-bonded interactions that include long-ranged Coulombic interactions and short ranged vdW interactions. To reduce the computational cost of simulations, vdW interactions at distances longer than an explicitly defined cutoff distance are not included. In this dissertation, the vdW cutoff distance was 1.0 nm for all simulations. Coulombic interactions may be calculated beyond the vdW cutoff distance, which in this work is only done for systems involving charged particles. In this case, the Particle-mesh Ewald (PME) method^{40,41} is used to calculate Coulombic potentials more efficiently than explicit calculation of Coulombic potential between each atom pair. Explicit solvent molecules are used throughout this dissertation, with the TIP3P water model used for all simulations. The integration time step is 2 fs for all calculations.

UMBRELLA SAMPLING

Umbrella sampling is a technique to calculate free energy along a reaction coordinate by biased MD simulations⁴². In the case of the charged spherical NPs studied in this dissertation, the reaction coordinate is the center-to-center distance between two charged NPs. Systems containing two charged NPs subject to a harmonic restraining potential at a given reaction coordinate are prepared at 1 Å intervals and simulated by MD. The variation of the reaction coordinate during the simulation is used to determine the free energy profile by the weighted histogram analysis method (WHAM)^{43,44}.

Chapter 3: Nanocube immersion and clustering at the water-air interface

INTRODUCTION

Over the last two decades advances in experimental techniques have allowed the controlled synthesis of highly monodisperse NPs with a variety of compositions^{1,45}, sizes^{3,5}, and shapes⁶⁻¹¹. Many types of superstructures and superlattices have been prepared by the self-assembly of these NPs in bulk solution^{13,46}, on the surface of solutions¹⁴⁻¹⁸, and on various substrates⁴⁶. Materials prepared in this manner are of interest for their novel optical, catalytic, magnetic, electronic, sieving, and thermoelectric properties^{12,47-52}.

Studies of spherical NPs have shown that they can self-assemble on liquid surfaces to produce ultrathin single or binary superlattices (SLs, BNSLs). The structure formed by this process is determined by the immersion depth of NPs on the liquid surface¹⁶, which is itself dependent on the surface energy of the liquid and the strength of NP-liquid coupling interactions^{16,53}. Liquid-NP interactions include vdW, Coulombic, hydrophobic, and other interactions¹, all of which depend on the NP and solvent used as well as on any applied field or substrate present.

Anisotropic NPs, such as nanocubes (NCs), have the potential to form a wide variety of superstructures not accessible using spherical NPs. An analytical model of and MD simulations of NC immersion are used here to study NCs on liquid surfaces and the early stages of their self-assembly. Understanding the mechanisms underlying NP self-assembly is necessary to enable the rational design and synthesis of NP superlattices at liquid surfaces.

Below, I present my published research on the immersion and self-assembly of nanocubes at the water-air surface⁵⁴.

METHODS

Analytical model

Immersion of a ligated metal NC in diethylene glycol (DEG) requires the creation of excess liquid surface area, A_{excess} . Creation of excess surface area has a Gibbs free energy cost of $G_1 = \gamma A_{excess} = \gamma(A_{imm} - A_{slice})$, where A_{imm} is the contact area between the NC and DEG and A_{slice} is the surface area of the liquid displaced by NC immersion. For an NC in the flat orientation (Fig. 3.1)

$$A_{imm} = \begin{cases} a^2 + 4h^2, h < a \\ 2a^2 + 4h^2, h = a \end{cases} \quad (3.1)$$

and

$$A_{slice} = a^2 \quad (3.2)$$

where a is the NC edge length and h is the immersion height.

The energetic cost of increased liquid surface area is offset by favorable interactions between the liquid and the NC surface. These favorable interactions are evaluated as

$$G_2 = G^\circ A_{imm} \quad (3.3)$$

where G° is the free energy of NC-liquid interaction per unit area. For a dodecanethiol-passivated gold NC immersed in DEG, $G^\circ \approx -7 \text{ kcal/mol} \cdot \text{nm}^2$.^{2,16} Additional values of G° are used as defined in the legend of Fig. 3.1. The total Gibbs free energy of NC-liquid immersion as a function of immersion height is given by

$$\Delta G = G_1 + G_2. \quad (3.4)$$

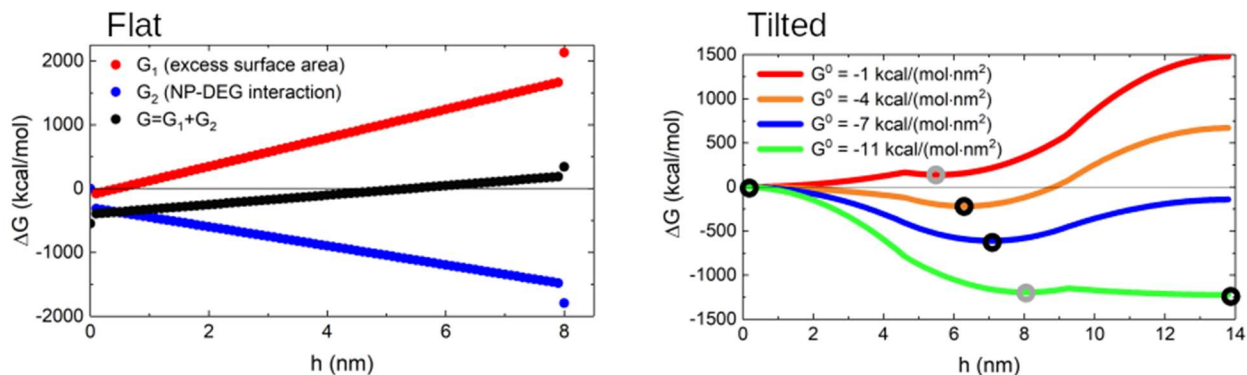


Figure 3.1: Analytical model of NP immersion. For the flat orientation minima are possible only at full immersion and zero immersion, while for the tilted orientation a local or global minimum near half immersion is observed.

MD simulations

The immersion of Au NCs at the liquid-air surface was investigated by atomistic MD simulations of Au NCs with varying surface vdW interactions. In all simulations, solid core NCs were prepared by cutting a face centered cubic lattice of Au atoms (Au-Au bond length of 2.88 Å) into NCs with either 3.07 nm or 5.1 nm edge lengths. The 3.07 nm NC model was used for simulations without explicit ligands, while the 5.1 nm NC model was used for simulations with thiolated ligands covalently bound to the NC facets via Au-S bonds with surface density of 0.3949 ligands per Au atom. Three ligands were studied: $-\text{S}(\text{CH}_2)_{11}\text{CH}_3$, $-\text{S}(\text{CH}_2)_{11}\text{OCH}_3$, and $-\text{S}(\text{CH}_2)_{12}\text{OH}$. All ligands were prepared using Gaussview and distributed on NC facets using our own code. Prepared NCs were solvated in TIP3P water using the solvate VMD plugin⁵⁵. In all cases the NCs were initially positioned halfway immersed at the water surface in a facet-down orientation.

Data analysis

NC-water contact area was calculated as a function of time,

$$a_{imm}(t) = \frac{1}{2} (a_{NC} + a_{sol}(t) - a_{tot}(t)) \quad (3.5)$$

where a_{NC} , $a_{sol}(t)$, and $a_{tot}(t)$ are the solvent accessible surface areas (SASA) of the NC, water, and NC-water system respectively. These values were calculated using the SASA built-in VMD plugin⁵⁵. For solid core NCs in tilted orientations, the average angle between the NC body diagonal and the vector normal to the surface of the water slab was calculated. NC body diagonals were taken to be the vector between the Au atom at one corner of the NC and the center of the 3 Au atoms at the opposite corner, where one of these corners is the most deeply immersed corner.

RESULTS

Analytical model of nanocube immersion

The analytical model of NC immersion was used to calculate the Gibbs free energy of an individual NC immersed in liquid following the procedure previously reported for spherical NPs¹⁶. Comparison of the free energy of the flat and tilted orientations is used to predict what orientation a particular NC will adopt. Immersion of an NC in a liquid produces a cavity in that liquid, thereby increasing the surface area of the liquid. The free energy cost of creating this surface area is dependent on the surface tension of the liquid, and is offset by favorable (mostly dispersive) interactions between liquid molecules and NC ligand molecules. Because free energy cost of immersion depends both on the contact area between the NC and liquid and on the surface area of liquid displaced by NC immersion (i.e. the cross-sectional area of the NC at the liquid surface), it is dependent on the orientation of the NC. The change in contact area with immersion height is itself dependent on the NC orientation, therefore the favorable energy of interaction between NC and liquid is also dependent on the NC orientation. This leads to equations 3.1-3.4 and the free energy profiles shown in figure 3.1. For NCs in the flat orientation, both the free energy cost of immersion $G_1 = \gamma(A_{imm} - A_{slice})$ and the favorable interaction energy $G_2 = G^\circ A_{imm}$ depend only on A_{imm} as A_{slice} is constant. A_{imm} is a linear function of immersion height and as a result G_1 , G_2 , and their sum $\Delta G = G_1 + G_2$ are all linear functions of immersion height. Because G_1 is always positive (i.e., unfavorable), G_2 is always negative (i.e., favorable), and the free energy

profile is linear, the minimum free energy must occur at an immersion height of either 0 or a , where a is the edge length of the NC as in equations 3.1-3.4. NCs in the flat orientation will therefore either fully immerse or sit on the liquid surface without immersing into it unless they reorient to the tilted orientation. In the tilted orientation, A_{imm} is again a function of immersion height and A_{slice} is also a function of immersion height rather than a constant as in the flat orientation. As a consequence of this, while G_2 is linear as in the flat case, G_1 is now nonlinear and a piecewise function. As a result, free energy profiles of NCs in the tilted orientation have a minimum between $h = \frac{\sqrt{3}}{3} a$ and $h = \frac{2\sqrt{3}}{3} a$. Depending on the surface tension of the liquid and the strength of NC-liquid binding interactions, this may be either a local or global free energy minimum as shown in figure 3.1. NCs where this is a local minimum will have a global minimum at either 0 immersion or full immersion as seen in the flat orientation, but in the case where this approximately half-immersed state is a global free energy minimum NCs will adopt the tilted orientation and partially immerse into the liquid.

MD simulations

The configurations of NCs on the water surface after equilibration are shown in figure 3.2A-C. For NCs with weak NC-water coupling (> -0.1 kcal mol), NCs sit on the water surface and do not immerse, while strong NC-water coupling (< -0.5 kcal mol) leads to complete immersion. Partial immersion and adoption of the tilted orientation is observed for NCs with intermediate NC-water coupling (-0.45 kcal mol $< < -0.1$ kcal mol), with the immersed area positively correlated with coupling strength as shown in figure 3.2G. This correlation is similar to that previously reported for spherical NPs¹⁶. The body diagonals of the NCs are not aligned with the vector normal to the water surface, instead being misaligned by 4.5° – 6.7° as shown in figure 3.2H. Simulations of NCs passivated with organic ligands of varying hydrophobicity revealed that each of the immersion states predicted is accessible with real ligands. The NCs, shown after equilibration in figure 3.2D-F, were coated with hydrophobic (dodecane-1-thiol, $-\text{S}(\text{CH}_2)_{11}\text{CH}_3$),

moderately hydrophobic (11-methoxyundecane-1-thiol, $-\text{S}(\text{CH}_2)_{11}\text{OCH}_3$), or hydrophilic (12-mercaptododecan-1-ol, $-\text{S}(\text{CH}_2)_{12}\text{OH}$) ligands. Au@dodecane-1-thiol NCs do not immerse, Au@11-methoxyundecane-1-thiol NCs partially immerse in tilted orientations, and Au@12-mercaptododecan-1-ol NCs immerse during equilibration at the water surface. The Au@12-mercaptododecan-1-ol NCs do not fully immerse due to parting of ligands at the NC edges that exposes the hydrophobic alkyl region of the ligands (Fig. 3.2F). Following simulations of single NCs at the water surface, systems of 2-4 naked NCs ($\epsilon = -0.3$ kcal mol) were prepared and equilibrated to investigate the clustering behavior of NCs in the tilted orientation. NCs were initially placed halfway immersed at the water surface in the flat orientation in linear, L-shaped, staggered, or shifted arrangements with slight separation between NCs as shown in figure 3.3 (insets). NCs quickly reoriented to the tilted orientation upon the start of equilibration, following which they approached each other via diffusion and formed stable aggregates (figure 3.3) via binding interactions between neighboring facets. Individual NCs showed slight shifting or rotation of facet to facet contacts (figure 3.3A, middle, and figure 3.3B, right, respectively) rather than perfect overlap of facets, which would maximize the interactions between NCs. Aggregates of NCs favored tilted orientations, where the immersion of each NC depends on its position within the aggregate. Similar configurations are expected for larger aggregates of NCs, though without the tilted orientation of the complete aggregate. Self-assembly of NCs into larger superlattices is governed by the same principles, and this behavior suggests the possibility of forming "Janus-type" superlattices where a more hydrophilic NC forms an immersed layer and an intermediate NC forms a layer above it.

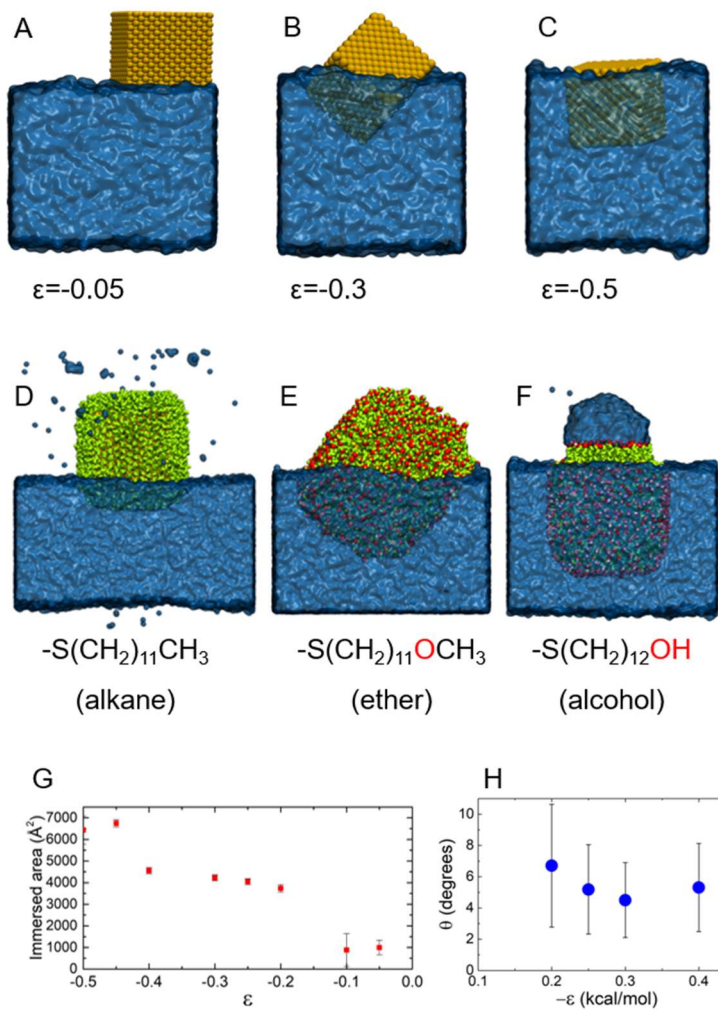


Figure 3.2: Configurations of A) hydrophobic NC, B) moderately hydrophilic NC, and C) hydrophilic NC on water (transparent blue surface) surface after 100 ns MD simulation. D-F) Configurations of NCs with similar hydrophobicity to A-C but with explicit ligands (C atoms shown in green, O atoms in red, and H atoms not shown for clarity). G) Immersed area of naked NCs as a function of ϵ . H) Angle between naked NC body diagonal and vector normal to liquid surface as function of ϵ . NC immersion depends on the hydrophobicity of the NC.

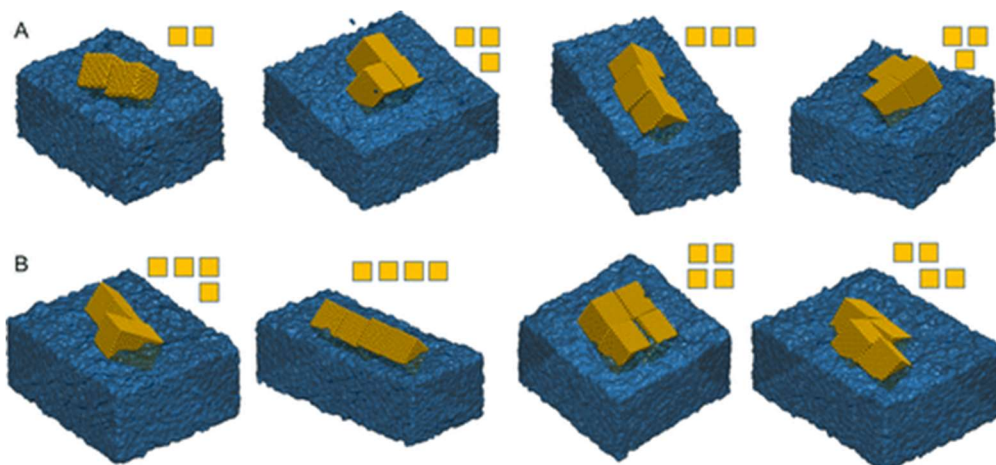


Figure 3.3: A) Configurations of two or three NC clusters ($\epsilon = -0.3$ kcal/mol) in different initial arrangements (insets). In the initial states, the NCs have 45 or 50 Å center-to-center distances. B) Configurations of four NC clusters ($\epsilon = -0.3$ kcal/mol) in different initial arrangements (insets). In the initial state, the NCs have 45 Å center-to-center distances. All images are obtained after 100 ns of equilibration.

CONCLUSIONS

As expected, NCs which show very strong NC-liquid binding interactions will immerse fully, resulting in bulk solution behavior, while NCs where NC-liquid binding energy is small relative to the surface energy of the liquid will not immerse into the liquid. However, there is an intermediate regime where NC-liquid binding is strong enough for the approximately half-immersed free energy minimum to be lower in energy than 0 immersion but not strong enough for full immersion to be favored. This results in a global free energy minimum at approximately half immersion and NCs which show this NC-liquid binding will adopt the tilted orientation and immerse partway into the liquid. The self-assembly of NCs is dependent on the immersion behavior of the NCs, which is determined by the liquid surface energy and the strength of NC-liquid interactions.

Chapter 4: Self-assembly of super-charged nanospheres in ionic solution

INTRODUCTION

The assembly of NPs into superlattices is of interest both at interfaces, as discussed in Chapter 3, and in the bulk as described in the present chapter. The assembly of charged NPs in solution is also of interest because charged NPs can assemble into superlattices with structures determined by electrostatics rather than the vdW or hard-sphere interactions that drive the assembly of neutral NPs^{20,22}. Because electrostatic interactions may be either attractive or repulsive, in contrast to the always-attractive nature of vdW and hard-sphere interactions, this allows the synthesis of NP superlattices with non-close-packed structures²². Unlike lattices of small (atomic or molecular) ions, the stoichiometry of superlattices formed by charged NPs is not dictated by charge neutrality, as a result of screening by ions in solution¹⁹. This allows the preparation of BNSLs with novel structures and resulting novel optical^{19,20,22}, catalytic^{20,22}, magnetic, and mechanical²⁰ properties. The structure formed by self-assembly of charged NPs is dependent on the size of the NPs, their core materials, their charge density and overall charge, and the ionic strength of the solution in which they assemble¹⁹. Manipulation of one or more of these properties allows control over the resulting SLs and is of significant experimental interest^{19,20,22}. Understanding how these properties govern the self-assembly of charged NPs is crucial to enabling the rational design and synthesis of BNSLs formed by self-assembly of charged NPs. Here, a system of super-charged spherical NPs in a solution with relatively high ionic strength is considered. NPs are dispersed in a concentrated solution of $(\text{NH}_4)_2\text{CO}_3$ and form SLs as the ions evaporate from the solution. Because SL formation begins when the ionic strength of the solution is still relatively high, NP interactions take the form of a surface-centered Yukawa type potential due to screened Coulombic coupling between charged tips of ligands. Longer range Coulombic coupling is screened by the ionic solution.

METHODS

Geometric criterion for superlattice structure

Based on a pure geometry/energy criterion, charged NPs will form a particular lattice if the lattice constants and NP size ratio allow oppositely charged NPs to be in direct contact with each other. NPs will thus form a lattice which satisfies this criterion or, should no lattice be favorable, form an amorphous aggregate. For the CsCl lattice (figure 4.1A), the center-to-center distance between two similarly charged particles is d and for two oppositely charged particles it is $\frac{\sqrt{3}}{2} d$. For a size ratio $d_A:d_B$ where $d_A > d_B$, a CsCl lattice can be formed only when $d_A:d_B$ is less than 1.366:1, as greater size ratios do not allow B particles to contact neighboring A particles even when A particles are in direct contact with each other. Similarly to the CsCl lattice, a hexagonal lattice (figure 4.1B) should form when the lattice constant and NP size ratio allow oppositely charged NPs to be in direct contact with each other. For the hexagonal lattice, the center-to-center distance between two A particles is the lattice constant f and for two dissimilar NPs it is $h = \frac{\sqrt{21}}{6} f$. For size ratios $d_A:d_B$ larger than 1.9:1, contact between oppositely charged NPs is not possible even when A particles are in direct contact. Using the same arguments as for the CsCl lattice, the hexagonal lattice cannot be formed at size ratios larger than 1.9:1. Finally, a Th_3P_4 lattice (figure 4.1C) may be formed when the NP size ratio and the Th_3P_4 lattice constants d_{A-A} and d_{A-B} allow direct contact between oppositely charged NPs but the CsCl and hexagonal lattice constants would not. Based on the distances between A (large) particles and B (small) particles shown in figure 4.1c, $d_{A-A} = 4.03631$ and $d_{A-B} = 2.9869$ units, the Th_3P_4 lattice will fail to form when $\frac{d_A}{d_B} > \frac{d_A}{2.9869 - \frac{d_A}{2}} = 2.083$, leading to the formation of an amorphous aggregate when $d_A:d_B > 2.083:1$.

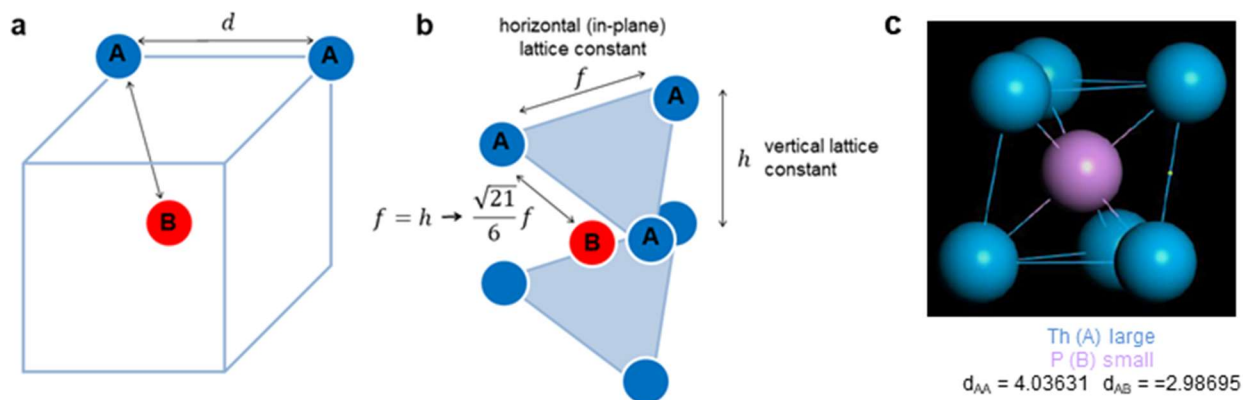


Figure 4.1: Scheme of A) CsCl, B) hexagonal, and C) Th₃P₄ lattices showing their respective lattice constants.

Numerical model of superlattice structure using free energy profiles

Spherical Au NP cores with diameter 5 nm were prepared in VMD and covered with either 11-mercaptopundecanoic acid (MUA) or 70% (11-mercaptopundecyl)-N,N,N-trimethylammonium (TMA)/30% 1-hexanethiol ligands^{56–58} (Au@TMA) using our own code. For NPs with MUA ligands (Au@MUA), 50% of ligands were protonated (neutral) and 50% were deprotonated (negative). Each NP was covered with 382 randomly placed ligands, placed in a solution of 4.28 M (NH₄)₂CO₃ (the concentration at which the start of NP self-assembly is observed) prepared using a combination of the VMD autoionize plugin⁵⁵ and our own code. TIP3P water molecules were added using the VMD solvate plugin. All interactions were defined by the CHARMM general force field^{59,60} with ligand parameters determined using the CGenFF ParamChem web server^{59,61}. Free energy profiles were obtained using umbrella sampling (US) and the weighted histogram analysis method (WHAM)^{43,44}. All MD simulations used for US were performed in the NpT ensemble using NAMD2.12 software³⁵. US simulations were performed at a pressure of 1 bar and temperature of 310 K with a Langevin constant of 0.01 ps⁻¹, a time step of 1.8 fs, and evaluation of long-range interactions every 1 (vdW) and 2 (Coulombic) time steps. The particle-mesh Ewald (PME) method^{40,41} was used to calculate long-range Coulombic interactions. US simulations were performed with center-to-center distance as the reaction coordinate, a reaction coordinate of 1 Å

(with occasional simulations at 0.5 Å intervals to ensure adequate histogram overlap), NP core centers of mass restrained to their initial positions using a harmonic potential with a spring constant of $1 \frac{kcal}{mol \text{ \AA}^2}$, and a total equilibration time of 10 ns. Images of the simulated systems were prepared using VMD. US was performed to determine free energy profiles of pairs of dissimilarly charged NPs and of similarly (positive or negative) charged NPs. Free energy profiles were used to calculate lattice free energies by counting the number of first and second neighbor contacts between NPs within the unit cell of each lattice and summing over the NP-NP interaction free energies for distances resulting from these contacts (see figure 4.2B). To obtain approximate interaction energies for pairs of NPs with diameters other than $d_A = d_B = 5 \text{ nm}$, energies were scaled by factors of $\frac{d_A d_B}{25 \text{ nm}^2}$, $\frac{d_A^2}{25 \text{ nm}^2}$, or $\frac{d_B^2}{25 \text{ nm}^2}$ to obtain the pairwise interaction energies E_{AB} , E_{AA} , and E_{BB} respectively. Surface energies were calculated as the cost to eliminate coupling between surface NPs and the would-be neighboring NPs that are not present due to the crystal surface.

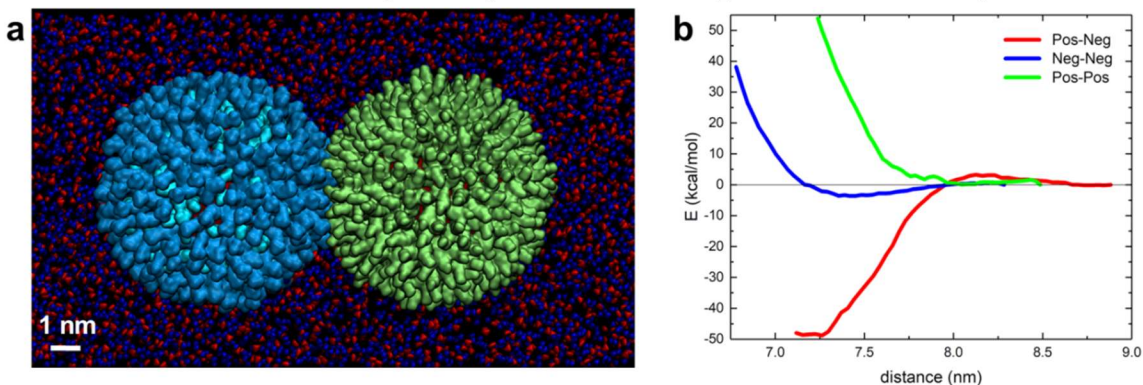


Figure 4.2: A) A pair of Au@TMA (left) and Au@MUA (right) NPs in 4.28 M $(\text{NH}_4)_2\text{CO}_3$ solution, after 22 ns of equilibration. TMA is shown in blue, 1-hexanethiol in cyan, MUA in green, NH_4^+ ions in dark blue, and CO_3^{2-} ions in red. NP cores are 5 nm in diameter and NPs are shown at a center-to-center distance of 7.3 nm. B) The free energy profiles of NP binding as calculated by US for each pair of NPs.

RESULTS

Geometric criterion for lattice formation

The predicted regions where each lattice is formed are shown in figure 4.3. The geometric criterion and experimental data are largely in agreement, but there are several experimental

structures which do not fit the geometric prediction. These outliers are the result of molecular details such as ligand flexibility that the simple geometric model does not consider, and a more accurate model can be constructed by numerical methods such as US.

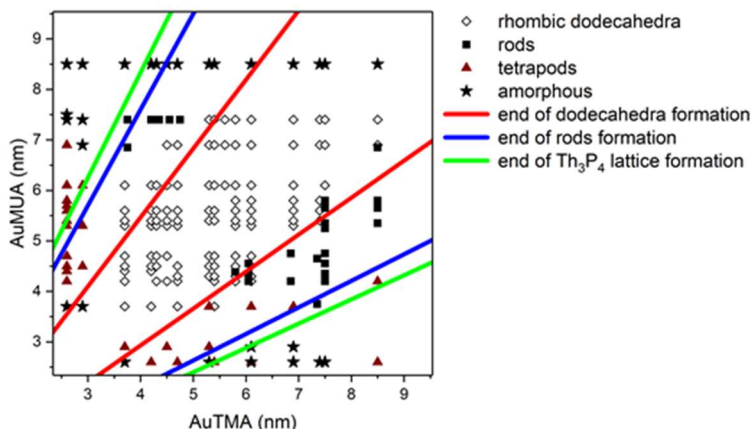
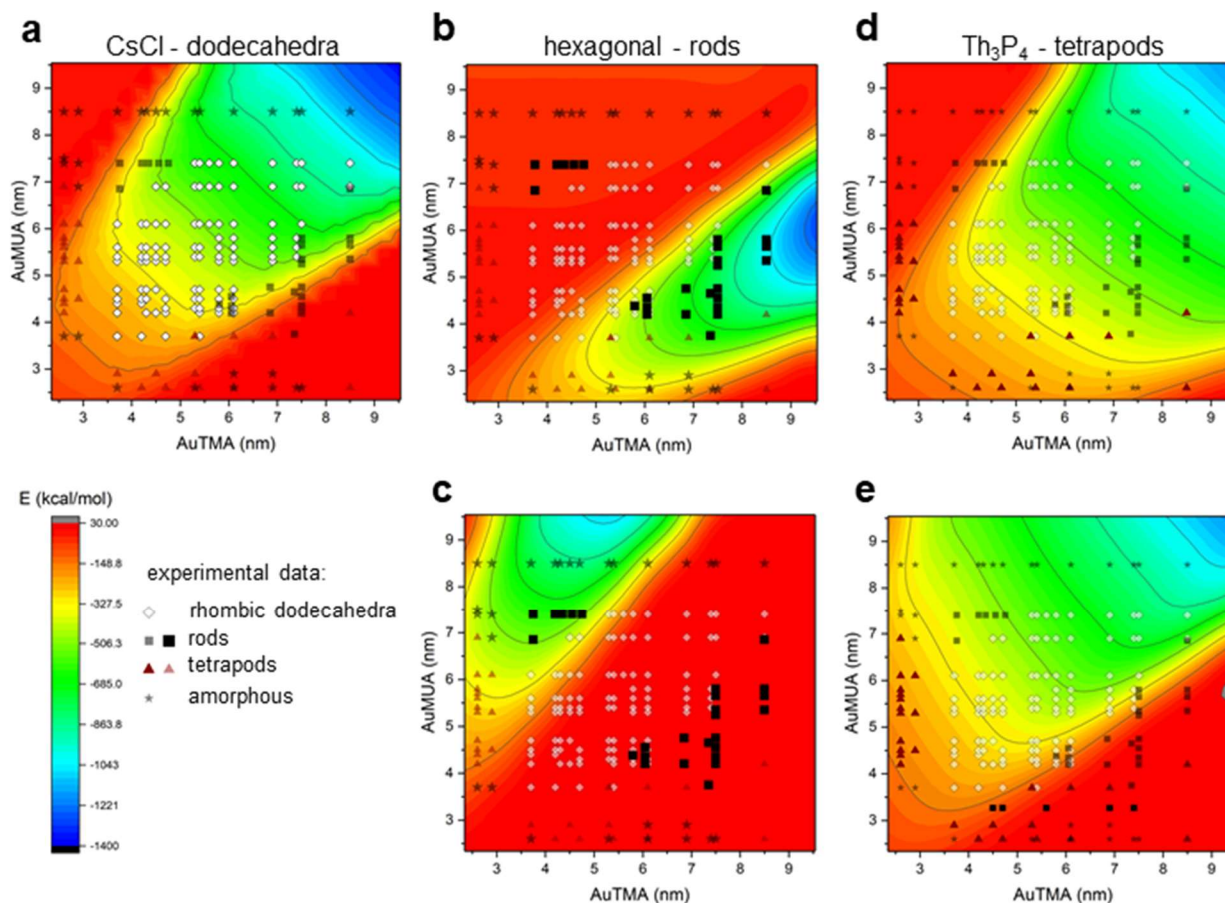


Figure 4.3: Phase diagram of self-assembled superlattice structures, obtained in experiment by Prof. Rafal Klajn's group (points) superposed with the line boundaries obtained by the geometric criteria analytical model. The variables are the sizes of the positively and negatively charged particles.

Numerical model of lattice formation based on Gibbs free energy

Free energy of binding between oppositely charged NPs in 4.28 M $(\text{NH}_4)_2\text{CO}_3$ solution has a local minimum of $\Delta G = -50 \text{ kcal/mol}$ at an NP separation of 7.1-7.25 nm, corresponding to NPs with ligand shells that are in direct contact. Because of the high ion concentration in the system, a very short screening length of $\lambda=0.1 \text{ nm}$ is calculated and NP interactions are essentially nonexistent at surface-to-surface distances greater than 0.8-1 nm. Because of this very short screening length, long-range Coulomb coupling is negligible and the SL structure is determined only by local (first and second neighbor) interactions, resulting in lattices similar to those formed by monatomic ions. The difference in free energy profile (figure 4.2B) between pairs of positive (Au@TMA) NPs and pairs of negative (Au@MUA) NPs is the result of the smaller number of MUA ligands which are charged, as well as the different ligand structure and differing interaction with NH_4^+ and CO_3^{2-} counter ions. Because of this difference, separate calculations were

performed with Au@TMA (positive) NPs as the larger NPs in A positions and smaller Au@MUA (negative) NPs in B positions, and with negative Au@MUA occupying A positions with smaller Au@TMA NPs occupying B positions. There is no difference for the CsCl lattice because A and B positions in that lattice are equivalent. The calculated lattice free energies (figure 4.4) again show better agreement with experimental data than does the geometric model. Additionally, unlike the geometric model the numerical model shows that formation of the CsCl lattice is energetically favorable for NPs which are close in size, while larger size differences favor formation of the hexagonal or Th_3P_4 lattices. While formation of the Th_3P_4 lattice is energetically favorable in the same region as the CsCl and hexagonal lattices, it is not the most energetically favorable lattice except when it is the only favorable structure. This explains both the boundaries between the CsCl, hexagonal, and Th_3P_4 lattices seen in experimental data as well as the numerous outliers, which



likely result from kinetic trapping.

Figure 4.4: Contour maps showing lattice free energy surfaces of (a) CsCl, (b-c) hexagonal, and (d-e) Th_3P_4 lattices, overlaid with experimental data from the Klajn group (points).

CONCLUSIONS

The phase diagram of spherical Au@MUA and Au@TMA NPs in 4.28 M $(\text{NH}_4)_2\text{CO}_3$ aqueous solution was developed by umbrella sampling and shows rough agreement with experimental data (figure 4.5). The majority of outliers can be explained by kinetic trapping in a lattice which is stable but not the most energetically favorable, as formation of such lattices is still more energetically favorable than remaining in solution or formation of an amorphous aggregate. However, this is not true of all outliers. These may be the result of the relatively large surface energy which is calculated for all of the observed crystals.

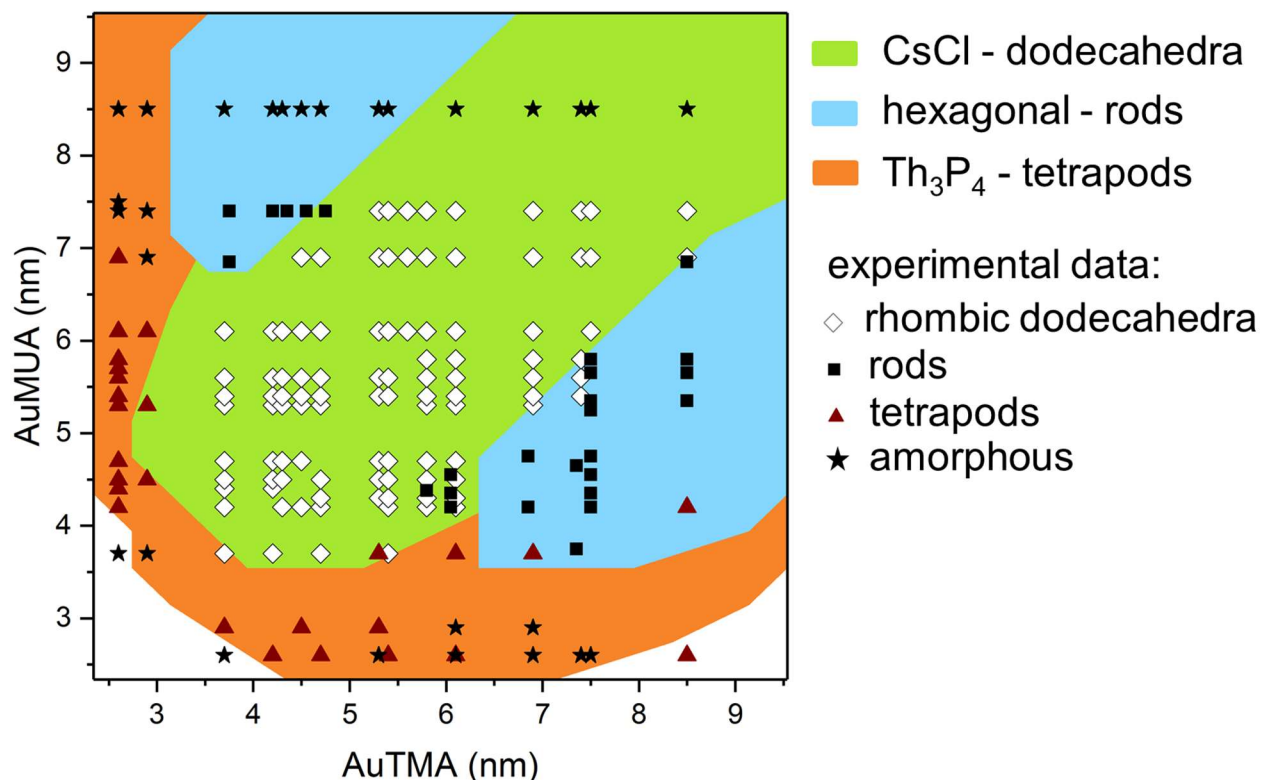


Figure 4.5: Phase diagram of SL formation by Au@MUA and Au@TMA NPs in aqueous 4.28 M $(\text{NH}_4)_2\text{CO}_3$ solution, overlaid with experimental data.

Chapter 5: Computational modeling of carbon nanotube-bound DNA-peptide conjugate nanosensors

INTRODUCTION

Use of semiconducting SWCNTs as building blocks for functional materials is an area of current interest, as the assembly of functional materials requires chemical modification of the SWCNT surface, and covalent modifications such as oxidation destroy their nIR fluorescence due to distortion of the conjugated π system³¹, making their use as biosensors challenging. Noncovalent functionalization with biological macromolecules preserves nIR fluorescence and produces a water-soluble complex despite the intrinsic hydrophobicity of SWCNTs⁶². Modifications such as wrapping of SWCNTs with ssDNA have been shown to produce fluorescent biosensors for reactive oxygen species, small molecules, neurotransmitters, nucleic acids, sugars, and proteins³²⁻³⁴. Here, I describe my use of MD simulations to understand the availability of a peptide bound to 1 or 2 ssDNA molecules for binding to $\alpha_{\text{IIb}}\beta_3$ integrin protein when (6,5)-SWCNTs are functionalized with the peptide-ssDNA hybrid.

METHODS

Classical atomistic MD simulations were performed to examine the structure and dynamics of ssDNA-RGD conjugates on SWCNTs. These simulations were used to determine the likely structures of these conjugates, calculate the exposure of RGD motifs to the solvent and potential binding partners, and analyze RGD dynamics. The simulated systems contained (6,5) SWCNTs wrapped with (GT)₅-RGD or (GT)₅-RGD-(GT)₅ molecules. The initial configurations of all simulations were generated by using Material Studio (Accelrys Software Inc. Materials Studio, Release 4.5; Accelrys Software Inc.: San Diego, CA, 2007) and visual MD (VMD) software⁵⁵. First, helical structures of ssDNAs were constructed by using Material Studio, and then, SWCNTs were wrapped with the helical ssDNAs by using VMD plugins. The systems were solvated and

ionized using the SOLVATE and IONIZE VMD plugins⁵⁵. The final systems contained approximately 73 000 ((GT)₅-RGD) and 95 500 ((GT)₅- RGD-(GT)₅) atoms. A salt concentration of 150 mM NaCl was selected to mimic physiological conditions. The CHARMM36 force-field parameters⁶³ and the TIP3P water model were used to define interactions for all the simulated molecules. The CHARMM general force field (Cgenff)³⁶ was used to model the organic linkers connecting ssDNA and RGD peptides. The NAMD2.12 package was employed to perform MD simulations³⁵. Long-range electrostatics were evaluated by the particle-mesh Ewald method^{40,41}. The evaluation of van der Waals and long-range Coulomb interactions was performed every 1 and 2 time steps, respectively; the timestep was set to 2 fs. All simulations were conducted in the NpT ensemble using periodic boundary conditions. Temperature and pressure remained constant at 300 K and 1 bar, respectively; the Langevin constant was set to $\gamma_{Lang} = 0.01 \text{ ps}^{-1}$. All the systems were initially minimized for 10 000 steps. After minimization and warming of the system, water and ions were equilibrated for 1 ns around the hybrid systems, which were restrained using harmonic forces with a spring constant of $1 \frac{\text{kcal}}{\text{mol \AA}^2}$. Then, the systems were equilibrated for 100 ns, while only SWCNTs were held restrained. Slightly different initial structures were selected from the trajectories obtained during system warming, and each system was run in three independent simulations. All the analyses were performed during the last 50 ns of production runs. Images of simulated systems were prepared with VMD. Solvent-exposed fraction of the RGD motif at time t was calculated using the formula

$$a_{SA} = 1 - \frac{a_{RGD}(t) + a_{DNA-SWCNT}(t) - a_{RGD-DNA-SWCNT}(t)}{2a_{RGD}(t)} \quad (5.1)$$

where $a_{RGD}(t)$, $a_{DNA-SWCNT}(t)$, and $a_{RGD-DNA-SWCNT}(t)$ are the solvent-accessible surface areas of the RGD motif, DNA and SWCNT, and the RGD-DNA-SWCNT complex, respectively, at time t . The evaluation was done by the SASA built-in VMD plugin³⁵, where the van der Waals radius of 1.4 Å was assigned to atoms to identify the points on a sphere that are accessible to the solvent. The solvent exposed fractions of RGDs reported in Figure 5.1c were

calculated by averaging the data obtained using equation 5.1. The dynamics of RGD motifs were evaluated by first calculating the Cartesian coordinates of RGDs centers of mass in time and then converting these coordinates into cylindrical coordinates r , θ , and z by means of our Tcl and Fortran codes. The choice of cylindrical coordinates for tracking the RGD dynamics was based on the symmetry of the simulated systems. Because SWCNTs are not completely covered by $(GT)_5$ -RGD or $(GT)_5$ -RGD- $(GT)_5$ molecules in the simulation setup, these molecules were free to translate and rotate on SWCNTs. Therefore, θ and z coordinates of the RGD center of mass reported in Figure 5.2 include the motion of RGD with respect to the DNA parts of molecules. To get pure dynamics of RGD motifs with respect to ssDNA anchors, translation and rotation of the whole $(GT)_5$ -RGD and $(GT)_5$ -RGD- $(GT)_5$ molecules were subtracted out.

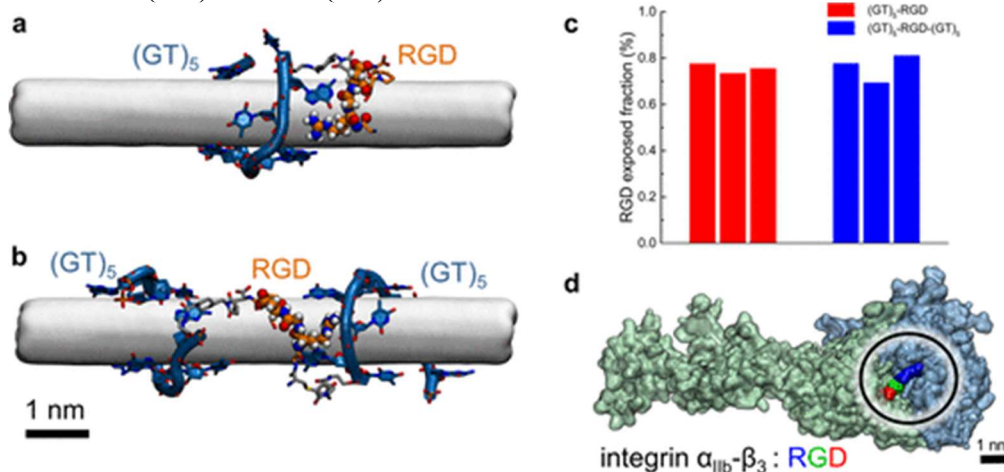


Figure 5.1: a) linear hybrid structure; b) bridged hybrid structure; c) RGD solvent exposed fraction; d) binding of RGD motif to integrin α_{11b} - β_3 .

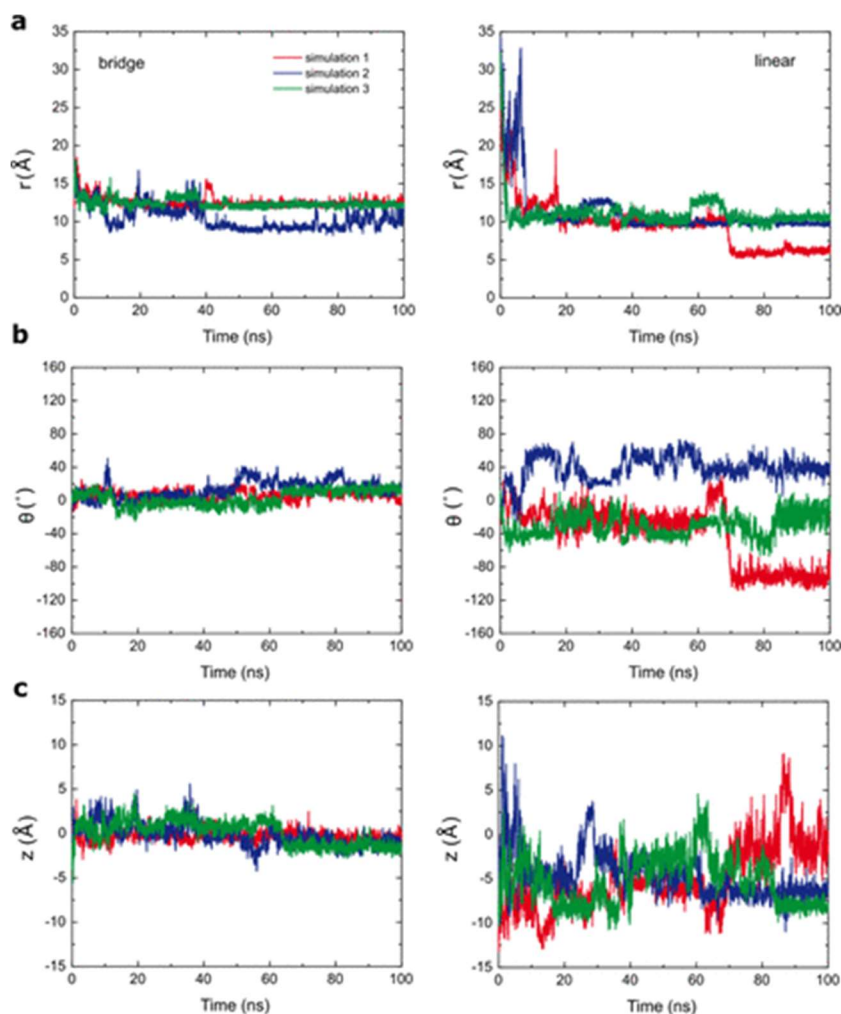


Figure 5.2: Plots of the normalized position of RGD in cylindrical coordinates, for a) r ; b) θ ; c) z . The r coordinate is correlated with RGD binding availability.

RESULTS

The solvent exposure of the RGD motif was analyzed for both systems in three independent simulations (Figure 5.1c). The RGD motif was mostly (70–80%) exposed to the solvent in all the cases, and thus available to bind to the integrin. The other 20–30% of the surface of the RGD motif interacted with SWCNT and ssDNA. This exposure of RGD should be sufficient for integrin binding because RGD binds into a shallow surface pocket of the integrin, as shown for the integrin α IIB β 3 in Figure 5.1d. The observed availability of RGD to bind to the integrin is in agreement with the binding observed in experiments⁶⁴.

According to experimental data, bridged hybrids exhibit higher binding affinity for $\alpha_{\text{IIB}}\beta_3$ integrin⁶⁴. However, all RGD motifs in molecules with helically wrapped ssDNAs are exposed to the solvent and available for integrin binding (Figure 5.1c). Instead, the differences in integrin binding could be due to differences in flexibility and conformational freedom of ssDNA–RGD conjugates. Therefore, the dynamics of RGDs in linear and bridge hybrids was examined. Figure 5.2 shows the dynamics of RGDs along three cylindrical coordinates r , θ , and z , which match the symmetry of the simulated systems. The RGD motifs had distinctly different dynamics in bridged versus linear hybrids. First, RGD motifs in bridged hybrids stayed rigid in θ and z dimensions because of being restrained by covalent bonds on both sides. On the other hand, RGD motifs in linear hybrids were very flexible and continuously changed their orientations with respect to ssDNA anchors. Second, RGD motifs in bridged hybrids did not fully approach the SWCNT surface, whereas RGD motifs in linear structures were able to adsorb fully onto the SWCNT (Figure 5.2a, simulation 1, where r approaches 6 Å). The results in Figure 5.2 show that RGDs in bridged hybrids remain available for binding, whereas the flexible RGDs in linear hybrids can engage in competitive binding with SWCNTs and ssDNA.

CONCLUSIONS

The availability of RGD in both linear and bridged hybrids was evaluated by calculating the solvent accessible surface area of RGD in each system. RGD is less flexible in the bridged hybrids, which while preventing some highly accessible conformations accessed by linear hybrids early in simulations also prevents RGD from interacting with ssDNA or the SWCNT by π - π stacking. As the experimental results published by Polo *et al*⁶⁴ show that CNTs bound to bridged hybrids have higher binding affinity to $\alpha_{\text{IIB}}\beta_3$ integrin than those bound to linear hybrids, the decreased flexibility of bridged hybrids leads to higher binding affinity by forcing RGD to adopt an integrin-accessible conformation without competitive interactions with ssDNA and the SWCNT.

References

- (1) Bishop, K. J. M.; Wilmer, C. E.; Soh, S.; Grzybowski, B. A. Nanoscale Forces and Their Uses in Self-Assembly. *Small* **2009**, *5* (14), 1600–1630. <https://doi.org/10.1002/sml.200900358>.
- (2) Albanese, A.; Tang, P. S.; Chan, W. C. W. The Effect of Nanoparticle Size, Shape, and Surface Chemistry on Biological Systems. *Annu. Rev. Biomed. Eng.* **2012**, *14* (1), 1–16. <https://doi.org/10.1146/annurev-bioeng-071811-150124>.
- (3) Mohamed, M. B.; Wang, Z. L.; El-Sayed, M. A. Temperature-Dependent Size-Controlled Nucleation and Growth of Gold Nanoclusters. *J. Phys. Chem. A* **1999**, *103* (49), 10255–10259. <https://doi.org/10.1021/jp9919720>.
- (4) Wang, J.; Neoh, K. G.; Kang, E. T. Preparation of Nanosized Metallic Particles in Polyaniline. *J. Colloid Interface Sci.* **2001**, *239* (1), 78–86.
- (5) Hussain, I.; Graham, S.; Wang, Z.; Tan, B.; Sherrington, D. C.; Rannard, S. P.; Cooper, A. I.; Brust, M. Size-Controlled Synthesis of Near-Monodisperse Gold Nanoparticles in the 1–4 Nm Range Using Polymeric Stabilizers. *J. Am. Chem. Soc.* **2005**, *127* (47), 16398–16399. <https://doi.org/10.1021/ja055321v>.
- (6) Yin, Y.; Alivisatos, A. P. Colloidal Nanocrystal Synthesis and the Organic-Inorganic Interface. *Nature* **2005**, *437* (7059), 664–670.
- (7) Min, Y.; Akbulut, M.; Kristiansen, K.; Golan, Y.; Israelachvili, J. The Role of Interparticle and External Forces in Nanoparticle Assembly. In *Nanoscience and Technology*; Co-Published with Macmillan Publishers Ltd, UK, 2008; pp 38–49. https://doi.org/10.1142/9789814287005_0005.
- (8) Tao, A. R.; Habas, S.; Yang, P. Shape Control of Colloidal Metal Nanocrystals. *Small* **2008**,

- 4 (3), 310–325. <https://doi.org/10.1002/sml.200701295>.
- (9) Srivastava, S.; Kotov, N. A. Nanoparticle Assembly for 1D and 2D Ordered Structures. *Soft Matter* **2009**, *5* (6), 1146–1156.
- (10) Chan, H.; Demortière, A.; Vuković, L.; Král, P.; Petit, C. Colloidal Nanocube Supercrystals Stabilized by Multipolar Coulombic Coupling. *ACS Nano* **2012**, *6* (5), 4203–4213. <https://doi.org/10.1021/nn3007338>.
- (11) Tan, S. F.; Raj, S.; Bisht, G.; Annadata, H. V; Nijhuis, C. A.; Král, P.; Mirsaidov, U. Nanoparticle Interactions Guided by Shape-Dependent Hydrophobic Forces. *Adv. Mater.* **2018**, *30* (16), 1707077. <https://doi.org/10.1002/adma.201707077>.
- (12) Shevchenko, E. V; Ringler, M.; Schwemer, A.; Talapin, D. V; Klar, T. A.; Rogach, A. L.; Feldmann, J.; Alivisatos, A. P. Self-Assembled Binary Superlattices of CdSe and Au Nanocrystals and Their Fluorescence Properties. *J. Am. Chem. Soc.* **2008**, *130* (11), 3274–3275. <https://doi.org/10.1021/ja710619s>.
- (13) Talapin, D. V; Shevchenko, E. V; Bodnarchuk, M. I.; Ye, X.; Chen, J.; Murray, C. B. Quasicrystalline Order in Self-Assembled Binary Nanoparticle Superlattices. *Nature* **2009**, *461*, 964.
- (14) Dong, A.; Chen, J.; Vora, P. M.; Kikkawa, J. M.; Murray, C. B. Binary Nanocrystal Superlattice Membranes Self-Assembled at the Liquid-Air Interface. *Nature* **2010**, *466*, 474.
- (15) Singh, G.; Chan, H.; Baskin, A.; Gelman, E.; Repnin, N.; Král, P.; Klajn, R. Self-Assembly of Magnetite Nanocubes into Helical Superstructures. *Science* (80-.). **2014**, *345* (6201), 1149.
- (16) Udayabhaskararao, T.; Altantzis, T.; Houben, L.; Coronado-Puchau, M.; Langer, J.;

- Popovitz-Biro, R.; Liz-Marzán, L. M.; Vuković, L.; Král, P.; Bals, S.; Klajn, R. Tunable Porous Nanoallotropes Prepared by Post-Assembly Etching of Binary Nanoparticle Superlattices. *Science* (80-.). **2017**, *358* (6362), 514–518. <https://doi.org/10.1126/science.aan6046>.
- (17) Miele, E.; Raj, S.; Baraissov, Z.; Král, P.; Mirsaidov, U. Dynamics of Templated Assembly of Nanoparticle Filaments within Nanochannels. *Adv. Mater.* **2017**, *29* (37), 1702682. <https://doi.org/10.1002/adma.201702682>.
- (18) Kim, D.; Bae, W. K.; Kim, S.-H.; Lee, D. C. Depletion-Mediated Interfacial Assembly of Semiconductor Nanorods. *Nano Lett.* **2019**, *19* (2), 963–970. <https://doi.org/10.1021/acs.nanolett.8b04198>.
- (19) Leunissen, M. E.; Christova, C. G.; Hynninen, A.-P.; Royall, C. P.; Campbell, A. I.; Imhof, A.; Dijkstra, M.; Van Roij, R.; Van Blaaderen, A. Ionic Colloidal Crystals of Oppositely Charged Particles. *Nature* **2005**, *437* (7056), 235.
- (20) Wang, L.; Albouy, P.-A.; Pileni, M.-P. Synthesis and Self-Assembly Behavior of Charged Au Nanocrystals in Aqueous Solution. *Chem. Mater.* **2015**, *27* (12), 4431–4440. <https://doi.org/10.1021/acs.chemmater.5b01370>.
- (21) Nagaoka, Y.; Tan, R.; Li, R.; Zhu, H.; Eggert, D.; Wu, Y. A.; Liu, Y.; Wang, Z.; Chen, O. Superstructures Generated from Truncated Tetrahedral Quantum Dots. *Nature* **2018**, *561* (7723), 378–382. <https://doi.org/10.1038/s41586-018-0512-5>.
- (22) Kalsin, A. M.; Fialkowski, M.; Paszewski, M.; Smoukov, S. K.; Bishop, K. J. M.; Grzybowski, B. A. Electrostatic Self-Assembly of Binary Nanoparticle Crystals with a Diamond-Like Lattice. *Science* (80-.). **2006**, *312* (5772), 420–424. <https://doi.org/10.1126/science.1125124>.

- (23) Dresselhaus, M. S.; Dresselhaus, G.; Saito, R. Physics of Carbon Nanotubes. *Carbon N. Y.* **1995**, *33* (7), 883–891. [https://doi.org/10.1016/0008-6223\(95\)00017-8](https://doi.org/10.1016/0008-6223(95)00017-8).
- (24) Dresselhaus, M. S.; Dresselhaus, G.; Saito, R.; Jorio, A. Exciton Photophysics of Carbon Nanotubes. *Annu. Rev. Phys. Chem.* **2007**, *58* (1), 719–747. <https://doi.org/10.1146/annurev.physchem.58.032806.104628>.
- (25) Carlson, L. J.; Krauss, T. D. Photophysics of Individual Single-Walled Carbon Nanotubes. *Acc. Chem. Res.* **2008**, *41* (2), 235–243. <https://doi.org/10.1021/ar700136v>.
- (26) Bardhan, N. M. 30 Years of Advances in Functionalization of Carbon Nanomaterials for Biomedical Applications: A Practical Review. *J. Mater. Res.* **2017**, *32* (1), 107–127. [https://doi.org/DOI: 10.1557/jmr.2016.449](https://doi.org/DOI:10.1557/jmr.2016.449).
- (27) Hong, G.; Diao, S.; Antaris, A. L.; Dai, H. Carbon Nanomaterials for Biological Imaging and Nanomedicinal Therapy. *Chem. Rev.* **2015**, *115* (19), 10816–10906. <https://doi.org/10.1021/acs.chemrev.5b00008>.
- (28) Kruss, S.; Salem, D. P.; Vuković, L.; Lima, B.; Vander Ende, E.; Boyden, E. S.; Strano, M. S. High-Resolution Imaging of Cellular Dopamine Efflux Using a Fluorescent Nanosensor Array. *Proc. Natl. Acad. Sci. U. S. A.* **2017**, *114* (8), 1789–1794. <https://doi.org/10.1073/pnas.1613541114>.
- (29) Bachilo, S. M.; Strano, M. S.; Kittrell, C.; Hauge, R. H.; Smalley, R. E.; Weisman, R. B. Structure-Assigned Optical Spectra of Single-Walled Carbon Nanotubes. *Science* **2002**, *298* (5602), 2361–2366. <https://doi.org/10.1126/science.1078727>.
- (30) Smith, A. M.; Mancini, M. C.; Nie, S. Bioimaging: Second Window for in Vivo Imaging. *Nat. Nanotechnol.* **2009**, *4* (11), 710–711. <https://doi.org/10.1038/nnano.2009.326>.
- (31) Ghosh, S.; Bachilo, S. M.; Simonette, R. A.; Beckingham, K. M.; Weisman, R. B. Oxygen

- Doping Modifies Near-Infrared Band Gaps in Fluorescent Single-Walled Carbon Nanotubes. *Science* **2010**, *330* (6011), 1656–1659. <https://doi.org/10.1126/science.1196382>.
- (32) Kruss, S.; Landry, M. P.; Vander Ende, E.; Lima, B. M. A.; Reuel, N. F.; Zhang, J.; Nelson, J.; Mu, B.; Hilmer, A.; Strano, M. Neurotransmitter Detection Using Corona Phase Molecular Recognition on Fluorescent Single-Walled Carbon Nanotube Sensors. *J. Am. Chem. Soc.* **2014**, *136* (2), 713–724. <https://doi.org/10.1021/ja410433b>.
- (33) Harvey, J. D.; Jena, P. V.; Baker, H. A.; Zerze, G. H.; Williams, R. M.; Galassi, T. V.; Roxbury, D.; Mittal, J.; Heller, D. A. A Carbon Nanotube Reporter of MiRNA Hybridization Events In Vivo. *Nat. Biomed. Eng.* **2017**, *1*. <https://doi.org/10.1038/s41551-017-0041>.
- (34) Reuel, N. F.; Grassbaugh, B.; Kruss, S.; Mundy, J. Z.; Opel, C.; Ogunniyi, A. O.; Egodage, K.; Wahl, R.; Helk, B.; Zhang, J.; Kalcioğlu, Z. I.; Tvrđy, K.; Bellisario, D. O.; Mu, B.; Blake, S. S.; Van Vliet, K. J.; Love, J. C.; Wittrup, K. D.; Strano, M. S. Emergent Properties of Nanosensor Arrays: Applications for Monitoring IgG Affinity Distributions, Weakly Affined Hypermannosylation, and Colony Selection for Biomanufacturing. *ACS Nano* **2013**, *7* (9), 7472–7482. <https://doi.org/10.1021/nn403215e>.
- (35) Phillips, J. C.; Braun, R.; Wang, W.; Gumbart, J.; Tajkhorshid, E.; Villa, E.; Chipot, C.; Skeel, R. D.; Kalé, L.; Schulten, K. Scalable Molecular Dynamics with NAMD. *Journal of Computational Chemistry*. 2005. <https://doi.org/10.1002/jcc.20289>.
- (36) Vanommeslaeghe, K.; Hatcher, E.; Acharya, C.; Kundu, S.; Zhong, S.; Shim, J.; Darian, E.; Guvench, O.; Lopes, P.; Vorobyov, I.; Mackerell Jr, A. D. CHARMM General Force Field: A Force Field for Drug-like Molecules Compatible with the CHARMM All-Atom Additive

- Biological Force Fields. *J. Comput. Chem.* **2010**, *31* (4), 671–690.
<https://doi.org/10.1002/jcc.21367>.
- (37) Feller, S. E.; MacKerell, A. D. An Improved Empirical Potential Energy Function for Molecular Simulations of Phospholipids. *J. Phys. Chem. B* **2000**, *104* (31), 7510–7515.
<https://doi.org/10.1021/jp0007843>.
- (38) Klauda, J. B.; Venable, R. M.; Freites, J. A.; O'Connor, J. W.; Tobias, D. J.; Mondragon-Ramirez, C.; Vorobyov, I.; MacKerell, A. D.; Pastor, R. W. Update of the CHARMM All-Atom Additive Force Field for Lipids: Validation on Six Lipid Types. *J. Phys. Chem. B* **2010**, *114* (23), 7830–7843. <https://doi.org/10.1021/jp101759q>.
- (39) Verlet, L. Computer “Experiments” on Classical Fluids. II. Equilibrium Correlation Functions. *Phys. Rev.* **1968**, *165* (1), 201–214. <https://doi.org/10.1103/PhysRev.165.201>.
- (40) Darden, T.; York, D.; Pedersen, L. Particle Mesh Ewald: An N·log(N) Method for Ewald Sums in Large Systems. *J. Chem. Phys.* **1993**, *98* (12), 10089–10092.
<https://doi.org/10.1063/1.464397>.
- (41) Essmann, U.; Perera, L.; Berkowitz, M. L.; Darden, T.; Lee, H.; Pedersen, L. G. A Smooth Particle Mesh Ewald Method. *J. Chem. Phys.* **1995**. <https://doi.org/10.1063/1.470117>.
- (42) Kästner, J. Umbrella Sampling. *WIREs Comput. Mol. Sci.* **2011**, *1* (6), 932–942.
<https://doi.org/https://doi.org/10.1002/wcms.66>.
- (43) Kumar, S.; Rosenberg, J. M.; Bouzida, D.; Swendsen, R. H.; Kollman, P. A. THE Weighted Histogram Analysis Method for Free-Energy Calculations on Biomolecules. I. The Method. *J. Comput. Chem.* **1992**, *13* (8), 1011–1021.
<https://doi.org/https://doi.org/10.1002/jcc.540130812>.
- (44) Grossfield, A. WHAM: The Weighted Histogram Analysis Method. 2012.

- (45) Albanese, A.; Tang, P. S.; Chan, W. C. W. The Effect of Nanoparticle Size, Shape, and Surface Chemistry on Biological Systems. *Annu. Rev. Biomed. Eng.* **2012**, *14* (1), 1–16. <https://doi.org/10.1146/annurev-bioeng-071811-150124>.
- (46) Shevchenko, E. V; Talapin, D. V; Kotov, N. A.; O'Brien, S.; Murray, C. B. Structural Diversity in Binary Nanoparticle Superlattices. *Nature* **2006**, *439* (7072), 55–59.
- (47) Kang, Y.; Ye, X.; Chen, J.; Cai, Y.; Diaz, R. E.; Adzic, R. R.; Stach, E. A.; Murray, C. B. Design of Pt-Pd Binary Superlattices Exploiting Shape Effects and Synergistic Effects for Oxygen Reduction Reactions. *J. Am. Chem. Soc.* **2013**, *135* (1), 42–45. <https://doi.org/10.1021/ja3097527>.
- (48) Yang, Y.; Wang, B.; Shen, X.; Yao, L.; Wang, L.; Chen, X.; Xie, S.; Li, T.; Hu, J.; Yang, D.; Dong, A. Scalable Assembly of Crystalline Binary Nanocrystal Superparticles and Their Enhanced Magnetic and Electrochemical Properties. *J. Am. Chem. Soc.* **2018**, *140* (44), 15038–15047. <https://doi.org/10.1021/jacs.8b09779>.
- (49) Chen, J.; Dong, A.; Cai, J.; Ye, X.; Kang, Y.; Kikkawa, J. M.; Murray, C. B. Collective Dipolar Interactions in Self-Assembled Magnetic Binary Nanocrystal Superlattice Membranes. *Nano Lett.* **2010**, *10* (12), 5103–5108. <https://doi.org/10.1021/nl103568q>.
- (50) Urban, J. J.; Talapin, D. V; Shevchenko, E. V; Kagan, C. R.; Murray, C. B. Synergism in Binary Nanocrystal Superlattices Leads to Enhanced P-Type Conductivity in Self-Assembled PbTe/Ag₂Te Thin Films. *Nat. Mater.* **2007**, *6*, 115.
- (51) Cargnello, M.; Johnston-Peck, A. C.; Diroll, B. T.; Wong, E.; Datta, B.; Damodhar, D.; Doan-Nguyen, V. V. T.; Herzing, A. A.; Kagan, C. R.; Murray, C. B. Substitutional Doping in Nanocrystal Superlattices. *Nature* **2015**, *524*, 450.
- (52) Ibanez, M.; Luo, Z.; Genç, A.; Piveteau, L.; Ortega, S.; Cadavid, D.; Dobrozhan, O.; Liu,

- Y.; Nachtegaal, M.; Zebarjadi, M.; Arbiol, J.; Kovalenko, M. V; Cabot, A. High-Performance Thermoelectric Nanocomposites from Nanocrystal Building Blocks. *Nat. Comm.* **2016**, *7*, 10766.
- (53) Vuković, L.; Král, P. Coulombically Driven Rolling of Nanorods on Water. *Phys. Rev. Lett.* **2009**, *103* (24), 246103.
- (54) Nitka, T. A.; Král, P.; Vuković, L. Configurations of Nanocubes Floating and Clustering on Liquid Surfaces. *J. Phys. Chem. Lett.* **2019**, *10* (13). <https://doi.org/10.1021/acs.jpcclett.9b01638>.
- (55) Humphrey, W.; Dalke, A.; Schulten, K. VMD: Visual Molecular Dynamics. *J. Mol. Graph.* **1996**. [https://doi.org/10.1016/0263-7855\(96\)00018-5](https://doi.org/10.1016/0263-7855(96)00018-5).
- (56) He, J.; Lin, X.-M.; Chan, H.; Vuković, L.; Král, P.; Jaeger, H. M. Diffusion and Filtration Properties of Self-Assembled Gold Nanocrystal Membranes. *Nano Lett.* **2011**, *11* (6), 2430–2435. <https://doi.org/10.1021/nl200841a>.
- (57) Bera, M. K.; Chan, H.; Moyano, D. F.; Yu, H.; Tatur, S.; Amoanu, D.; Bu, W.; Rotello, V. M.; Meron, M.; Král, P.; Lin, B.; Schlossman, M. L. Interfacial Localization and Voltage-Tunable Arrays of Charged Nanoparticles. *Nano Lett.* **2014**, *14* (12), 6816–6822. <https://doi.org/10.1021/nl502450j>.
- (58) Zhao, H.; Sen, S.; Udayabhaskararao, T.; Sawczyk Michałand Kučanda, K.; Manna, D.; Kundu, P. K.; Lee, J.-W.; Král, P.; Klajn, R. Reversible Trapping and Reaction Acceleration within Dynamically Self-Assembling Nanoflasks. *Nat. Nanotechnol.* **2016**, *11* (1), 82.
- (59) Vanommeslaeghe, K.; MacKerell, A. D. Automation of the CHARMM General Force Field (CGenFF) I: Bond Perception and Atom Typing. *J. Chem. Inf. Model.* **2012**, *52* (12), 3144–3154. <https://doi.org/10.1021/ci300363c>.

- (60) Yu, W.; He, X.; Vanommeslaeghe, K.; MacKerell Jr., A. D. Extension of the CHARMM General Force Field to Sulfonyl-Containing Compounds and Its Utility in Biomolecular Simulations. *J. Comput. Chem.* **2012**, *33* (31), 2451–2468. <https://doi.org/10.1002/jcc.23067>.
- (61) Vanommeslaeghe, K.; Raman, E. P.; MacKerell, A. D. Automation of the CHARMM General Force Field (CGenFF) II: Assignment of Bonded Parameters and Partial Atomic Charges. *J. Chem. Inf. Model.* **2012**, *52* (12), 3155–3168. <https://doi.org/10.1021/ci3003649>.
- (62) Polo, E.; Kruss, S. Impact of Redox-Active Molecules on the Fluorescence of Polymer-Wrapped Carbon Nanotubes. *J. Phys. Chem. C* **2016**, *120* (5), 3061–3070. <https://doi.org/10.1021/acs.jpcc.5b12183>.
- (63) Best, R. B.; Zhu, X.; Shim, J.; Lopes, P. E. M.; Mittal, J.; Feig, M.; MacKerell, A. D. Optimization of the Additive CHARMM All-Atom Protein Force Field Targeting Improved Sampling of the Backbone ϕ , ψ and Side-Chain X1 and X2 Dihedral Angles. *J. Chem. Theory Comput.* **2012**. <https://doi.org/10.1021/ct300400x>.
- (64) Polo, E.; Nitka, T. T.; Neubert, E.; Erpenbeck, L.; Vukovic, L.; Kruss, S. *Control of Integrin Affinity by Confining RGD Peptides on Fluorescent Carbon Nanotubes*; 2018. <https://doi.org/10.1021/acsami.8b04373>.

Vita

Tara Allison Tyler Nitka earned her Bachelor of Science in chemistry from the Colorado School of Mines in 2016, where she worked on the experimental synthesis and analysis of catalytic nanomaterials. She joined the Department of Chemistry and Biochemistry at the University of Texas at El Paso in 2017, where her primary research focus is the investigation of nanoparticles self-assembly into novel materials for various applications, often done in close collaboration with experimental laboratories. Her research is performed by theoretical and computational chemistry techniques, and often involves writing new codes and the use of high-performance computing resources. Her research has so far resulted in one first author article, Configurations of Nanocubes Floating and Clustering on Liquid Surfaces, (DOI:[10.1021/acs.jpcclett.9b01638](https://doi.org/10.1021/acs.jpcclett.9b01638)) and two coauthored articles, “Control of Integrin Affinity by Confining RGD Peptides on Fluorescent Carbon Nanotubes” (DOI:[10.1021/acsami.8b04373](https://doi.org/10.1021/acsami.8b04373)) and “Effects of Metal Composition and Ratio on Peptide-Templated Multimetallic PdPt Nanomaterials” (DOI:[10.1021/acsami.6b11651](https://doi.org/10.1021/acsami.6b11651)).

Contact Information (optional) : tnitka@miners.utep.edu, taranitka@gmail.com